Determination of pressure in aqueo-carbonic fluid inclusions at high temperatures from measured Raman frequency shifts of CO_2

(Revision 5)

Xueyin Yuan[1,2], Robert A. Mayanovic[3], Haifei Zheng[1*], Qiang Sun[1]

[1] Key Laboratory of Orogenic Belts and Crustal Evolution, Ministry of Education, Peking University, Beijing 100871, China

[2] MLR Key Laboratory of Metallogeny and Mineral Assessment, Institute of Mineral Resources, Chinese Academy of Geological

Sciences, Beijing 100037, China

[3] Department of Physics, Astronomy and Material Science, Missouri State University, Springfield, MO 65897, USA

Abstract: Due to the presence of additional volatiles and/or electrolytes in CO_2-H_2O fluids, the total pressure of many natural aqueo-carbonic fluid inclusions at high temperatures as determined using microthermometry is usually made with considerable uncertainty. In this paper, we present the results of our high p-T in-situ Raman scattering study of high-density aqueo-carbonic fluids, with and without a small amount of CH_4 and NaCl, whose objective is to derive a new method for pressure determination in aqueo-carbonic fluid inclusions at high temperatures. The measurement of the Fermi diad bands at temperatures up to 400 °C and pressures up to 1200 MPa is described. The manner in which the frequency shifts and intensity of Raman bands are governed by pressure, temperature, presence of CH_4 in carbonic and NaCl in aqueous fluids is discussed. From the monotonic dependence of the frequency shifts of the lower Fermi diad band v_- and the Fermi resonant splitting D ($D = v_+ - v_-$) with pressure and temperature, the pressure (in MPa) of aqueo-carbonic fluid inclusions at elevated temperatures can be determined directly by using the following two polynomial equations:

$$p \text{ (MPa)} = -16 + 1.232 \times T - 53.72 \times (\Delta v_-) - 1.83 \times 10^{-3} \times T^2 + 24.46 \times (\Delta v_-)^2 - 0.292 \times T \times (\Delta v_-);$$

* Corresponding Author, Email: hfzheng@pku.edu.cn

23   p (MPa) $= -26 + 1.501 \times T + 193.24 \times (\Delta D) - 1.61 \times 10^{-3} \times T^2 + 5.436 \times (\Delta D)^2 + 0.158 \times T \times (\Delta D)$.

24   Where T is in °C, Δv_- and ΔD represent frequency shifts (in cm^{-1}) of the lower band and the resonant

25   splitting relative to the reference values measured at 23 °C and 6 MPa, respectively. Based on the

26   attainable accuracy of the fitted peak positions and the results from fitting of Raman frequency shifts'

27   dependence with pressure and temperature, the uncertainty in pressure determination is about 50

28   MPa for pressures determined from v_- and 40 MPa from that determined from D.

29   **Key words: CO$_2$, Raman spectroscopy, pressure determination, HDAC, fluid inclusion**

30

Introduction

32   Fluid inclusions containing H$_2$O-CO$_2$ fluids (aqueo-carbonic fluid inclusions) are very common

33   and are often the dominant fluid inclusion type occurring in hydrothermal and medium- to

34   high-grade metamorphic deposits (Chi et al., 2006; Lowenstern, 2001; Mumm et al., 1997; Phillips

35   and Evans, 2004; Thomas and Spooner, 1992; Tsunogae et al., 2002; Williams-Jones and Ferreira,

36   1989; Xu and Pollard, 1999). Determining the pressure of aqueo-carbonic fluid inclusions is of great

37   significance both in understanding their thermodynamic properties and in constraining the depth of

38   fluid activity and mineralization leading to trapping of the fluid inclusions. Presently, the principal

39   method of estimating the pressure in aqueo-carbonic fluid inclusions is by microthermometry, which

40   is based on measurements of two phase transition temperatures during heating, the liquid-vapor CO$_2$

41   homogenization temperature and the homogenization temperature of the immiscible-to-miscible

42   aqueous and carbonic phase transition, and use of the known p-V-T-x properties of the H$_2$O-CO$_2$

43   binary system (Bakker and Diamond, 2000; Diamond, 1996; Diamond, 2001; Hurai, 2010; Mao et al.,

44   2009). However, due to the presence of additional volatiles in the carbonic or electrolytes in the

45 aqueous phase in natural fluid inclusions (Berkesi et al., 2009; Bersani et al., 2009; Giorgetti et al.,

46 1996; Li et al., 2014; Peng et al., 2014; Salvioli-Mariani et al., 2015; Thomas et al., 1990; Wang et al.,

47 2013; Zhu and Peng, 2015), the phase transition temperatures in these aqueo-carbonic fluid

48 inclusions could be apparently different from those of the H_2O-CO_2 binary system (Akinfiev and

49 Diamond, 2010; Aranovich et al., 2010; Hurai, 2010; Mao et al., 2013; Shmulovich and Graham,

50 1999; Shmulovich and Graham, 2004; Thomas et al., 1990). In these cases, considerable errors in

51 pressure estimation using microthermometry can occur.

52   The Raman vibrational modes of CO_2 have been measured and interpreted (Gordon and

53 McCubbin, 1966; Rosso and Bodnar, 1995; Stoicheff, 1958), and based on the experiments that were

54 made in investigating the effects of temperature, pressure or density on CO_2 Raman peaks (Fig. 1),

55 the characteristic Fermi diad bands (v_+ and v_-) shift to lower frequencies, the resonant splitting ($D =$

56 $v_+ - v_-$) and the intensity ratio of the upper band to the lower band ($I(v_+)/I(v_-)$) increase monotonically

57 with increasing pressure or density (Fall et al., 2011; Garrabos et al., 1989; Garrabos et al., 1980;

58 Guo et al., 2014; Kawakami et al., 2003; Rosso and Bodnar, 1995; Song et al., 2009; Wang and

59 Wright, 1973; Wang et al., 2011; Welsh et al., 1952; Yamamoto and Kagi, 2006). Several attempts

60 have been made at ambient or low temperatures, in determining the pressure or CO_2 density in pure

61 CO_2 or H_2O-CO_2 fluid inclusions from the splitting of the two CO_2 Fermi diad bands (Azbej et al.,

62 2007; Chen et al., 2006; Fall et al., 2011; Kawakami et al., 2003; Rosso and Bodnar, 1995; Schmidt

63 et al., 1995; Song et al., 2009; Thomas et al., 1990; Yamamoto et al., 2007). However, to our

64 knowledge no investigation of the dependence of the CO_2 Fermi diad band frequencies with

65 variations of both pressure and temperature to high pressure-temperature (p-T) conditions has been

66 made. Here we present results from our high p-T Raman spectroscopy investigations of

67   H_2O-CO_2-NaCl, H_2O-CO_2-CH_4 and H_2O-CO_2-CH_4-NaCl systems, in order to determine the

68   dependence of the CO_2 Fermi diad band frequencies with pressure and temperature, and to study the

69   effects on these bands due to the presence of CH_4 in high-density carbonic and NaCl in aqueous

70   fluids. From these investigations, we have derived a new geobarometry for determining the total

71   pressure of aqueo-carbonic fluid inclusions at room to 400 °C temperature conditions.

Experimental apparatus and procedures

Hydrothermal diamond cell

74   A Bassett-type (Bassett et al., 1993) hydrothermal diamond anvil cell (HDAC) was used to

75   perform our Raman experiments. Two opposed diamond anvils with 800 μm diameter culets were

76   mounted on tungsten carbide seats and heated externally using molybdenum heaters wound around

77   the seats. The sample chamber was made by sealing a 400 μm diameter hole in the center of a 250

78   μm thick rhenium gasket against the anvils. The temperature was measured using two *K*-type

79   thermocouples attached to each of the diamond anvils and calibrated in advance by measuring the

80   melting point of stearic acid (69.6 °C) and sodium nitrate (307 °C) at ambient pressure. The pressure

81   in the sample chamber was determined either from the liquid-vapor equilibrium pressure of CO_2 at

82   low *p-T* conditions where vapor (V), carbonic liquid (L_{car}) and aqueous liquid (L_{aq}) coexisted, or

83   from the relative (to the value at ambient conditions) frequency shift of the 464 cm^{-1} Raman peak of

84   quartz at high *p-T* conditions (Schmidt and Ziemann, 2000):

85    $$p(\text{MPa}) = 0.36079 \times (v_{p,T} - v_{0,T})^2 + 110.86 \times (v_{p,T} - v_{0,T}) ;$$ (1a)

86    $$v_{0,T}\left(cm^{-1}\right) = v_{0,\,23°C} + 2.50136 \times 10^{-11} \times T^4 + 1.46454 \times 10^{-8} \times T^3 - 1.801 \times 10^{-5} \times T^2$$
$$- 0.01216 \times T + 0.29$$ (1b)

87   At low p-T conditions the pressure in the sample chamber was in fact the V+L_{car}+L_{aq} equilibrium

88   pressure of H_2O+CO_2±CH_4±NaCl systems, which differs slightly from the V+L equilibrium pressure

89   of pure CO_2. However, in comparison to the overall pressure uncertainty, the errors introduced by not

90   accounting explicitly for the partial pressure of dissolved H_2O and/or CH_4 in CO_2 are negligible. At

91   high p-T conditions the pressure determined from the quartz sensor yields the total pressure value,

92   with a reported pressure uncertainty of better than ±50 MPa based on an attainable accuracy of the

93   fitted Raman peak position of ±0.2 cm^{-1} (Schmidt and Ziemann, 2000).

Sample preparation

95   As gas-loading equipment is not readily available in our laboratory, the loading of CO_2 into the

96   aqueo-carbonic samples within the sample chamber of the hydrothermal diamond anvil cell was

97   accomplished using decomposition reactions described in greater detail below.

98   Decomposition of oxalic acid dihydrate ($H_2C_2O_4$·$2H_2O$) crystals in water (Sample I) and in NaCl

99   aqueous solution (Sample II) at high temperatures was accomplished as follows: Crystals of oxalic

100   acid dihydrate and quartz (for pressure calibration) were first loaded into the sample chamber,

101   followed by adding HPLC water (Sample I) or 10 wt% NaCl aqueous solution (Sample II; as H_2O

102   evaporated during sample loading whereas extra H_2O was generated from the decomposition of

103   oxalic acid dihydrate, the final NaCl concentration was not exact but around 10 wt%) just prior to

104   sealing of the sample chamber in the HDAC (Fig. 2a). During heating, the oxalic acid dehydrate

105   decomposed into H_2O, CO_2, CO and H_2 (Holloway et al., 1968; Wang and Zheng, 2012) at

106   approximately 250 °C (Fig. 2b), which was followed by generating CH_4 from the complete reaction

107   of CO and H_2 during further heating of the sample (I and II) to 600 °C. The composition of the

108   carbonic phase in Samples I and II, as estimated by use of the intensity ratio of the CO_2 and CH_4

109   Raman bands at room temperature and the quantification factor ratio given by Seitz et al. (1996), is

110   about 90 mol% CO_2 and 10 mol% CH_4 (Fig. 3).

111   Chemical reaction between sodium bicarbonate ($NaHCO_3$) and hydrochloric acid (HCl) in

112   aqueous solution (Sample III) was accomplished as follows: A sodium bicarbonate crystal and a

113   piece of quartz chip was firstly loaded inside the hole in the Re gasket positioned on top of the

114   bottom anvil, followed by the suspension of a small drop of 1.5 $mol \cdot L^{-1}$ hydrochloric acid aqueous

115   solution to the center of the face of the upper diamond anvil. The sample chamber of the HDAC was

116   subsequently quickly sealed by bringing the top anvil against the bottom anvil and gasket. Upon

117   contact and subsequent reaction of the sodium bicarbonate crystal and the hydrochloric acid solution,

118   CO_2 was generated and partly trapped within the sample chamber. The composition of the fluid

119   sealed in the sample chamber consisted of CO_2, H_2O, NaCl and potentially a small amount of

120   unreacted HCl. No Raman signal of HCO_3^- was detected.

121   **Raman measurement, spectral calibration and peak fitting**

122   All Raman measurements were made using a HORIBA Jobin Yvon confocal LabRAM HR800

123   micro-Raman system installed at Missouri State University. A 80 mW 785nm laser excitation source,

124   a Mitutoyo M Plan Apo NIR 20× long-working distance objective (NA = 0.4, f = 200), and a

125   stigmatic 800 mm spectrometer with a 2400 groove/mm grating were used to make the Raman

126   spectroscopy experiments. The confocal hole was set at 200 μm and the corresponding spectral

127   resolution was 0.5 cm^{-1} of the spectral measurements. Raman spectra were measured between 100

128   and 600 cm^{-1} and between 1000 and 1500 cm^{-1} for quartz and CO_2, respectively, using a counting

129   time of 60 seconds and by averaging 5 repeated collections.

130   In order to correct for peak position shifts during the experiment, 3 external (to the sample)

131   emission peaks occurring at 659.20, 865.32 and 888.44 cm^{-1} (Fig.3) and originating from a General

132   Electric 13-watt Energy Smart (model no. 74198) compact fluorescent lamp were collected

133   simultaneously at each p-T point for spectral calibration. The corrected peak positions (v_{corr}) were

134   spectrally calibrated from the Raman bands measured from the samples ($v_{measured}$) using:

135        $v_{corr} = v_{measured} - v_{light} + 804.32$ (2)

136   where v_{light} is the average value of the 3 peak positions. The consistency of v_{light} was verified in

137   advance by measuring the emission peaks simultaneously with the Raman band of a standard silicon

138   wafer at ambient temperatures ranging from 20 to 32 °C. Relative to the 520.70 cm^{-1} peak of silicon,

139   the variation in v_{light} was less than 0.10 cm^{-1} throughout the experiments.

140   Because of the fundamental dissimilarity between CO_2 and H_2O, and depending upon the p-T-X

141   conditions, CO_2 can present as a carbonic phase or phases (vapor, liquid, solid or clathrate hydrate)

142   or it can dissolve in the aqueous liquid of the CO_2-H_2O system (Diamond, 2001). In this study, a

143   separate, high-density (higher than the critical density of CO_2) carbonic phase was observed over a

144   wide pressure and temperature range. The p-T conditions and number of Raman spectra that were

145   measured for the samples are as follows: 27 spectra were measured from Sample I at p-T conditions

146   up to 250 °C and 900 MPa, 64 spectra were measured from Sample II at up to 400 °C and 1200 MPa,

147   and 18 spectra were measured from Sample III from 22 °C and 5 MPa to 193 °C and 284 MPa. The

148   peak center (with precision of 0.01 cm^{-1} after peak fitting) and intensity of the two Fermi diad bands

149   of CO_2 and the v_1 band of diamond were determined by fitting the Raman bands with Gauss-Lorentz

150   amplitude functions within the PeakFit V4.04 software package; the 464 cm^{-1} peak of quartz was

151   fitted with a Pearson IV amplitude function that permits variable peak asymmetry (Schmidt and

152   Ziemann, 2000), the three emission peaks used for v_{light} were fit consistently using Beta amplitude

153   functions. All iterative computations were carried out until the squared correlation coefficients $r^2 >$

154   0.99 were obtained. The uncertainties in frequency of the spectrally calibrated CO_2 Fermi diad bands

155   and the 464 cm^{-1} peak of quartz were ±0.1 and ±0.2 cm^{-1} at temperatures below and above 200 °C,

156   respectively.

157   **Results**

158   The representative Raman spectra measured with Sample I and II at room temperature are shown

159   in Figure 4. The frequency of the lower band (v_-) decreases monotonically with increasing pressure,

160   from 1281.56 cm^{-1} at 6 MPa to 1277.41 cm^{-1} at 698 MPa. Within the same pressure range, the

161   frequency of the upper band (v_+) also decreases with increasing pressure but varies by less than 1.2

162   cm^{-1}, and the magnitude of the resonance splitting (D) increases monotonically from 104.07 cm^{-1} at 6

163   MPa to 107.26 cm^{-1} at 698 MPa. The intensity of the upper Fermi diad band increased significantly

164   whereas that of the lower band remained nearly constant as the density of carbonic phase increased

165   with pressure. Our results are in good agreement with the Raman spectroscopy results obtained from

166   pure CO_2 at ambient temperature and high pressures (Garrabos et al., 1989; Kawakami et al., 2003;

167   Rosso and Bodnar, 1995; Song et al., 2009; Wang et al., 2011; Yamamoto and Kagi, 2006).

168   The temperature dependence of the frequency values of the Fermi diad bands, as measured at

169   *p-T* conditions ranging from 141 MPa at 23 °C to 474 MPa at 250 °C for Sample I, and from 124

170   MPa at 23 °C to 639 MPa at 350 °C for Sample II, and after accounting for the pressure dependence,

171   is shown in Figure 5. The lower Fermi diad band increases at a slightly higher $\partial v/\partial T$ rate than the

172   upper band and D exhibits a negative $\partial v/\partial T$ rate with increasing temperature, which is in agreement

173   with the temperature dependence of the Raman vibrations of pure CO_2 (Wang et al., 2011). The

174   intensity of two hot bands was found to increase with temperature to ~250 °C, and the intensity of all

175   observed Raman bands of CO_2 decreased significantly at temperatures higher than 300 °C (Fig. 5).

176   The overall p-T-dependent frequency shifts of v_-, v_+ and D in high-density carbonic fluids, are

177   given by the following polynomial equation (where the frequency of v_-, v_+ or D values is represented

178   by v):

179         $v\,(p,\,T) = v\,(p_0,\,T_0) + \Delta v\,(p,\,T) = a + b{\times}T + c{\times}p + d{\times}T^2 + e{\times}p^2 + f{\times}T{\times}p$ (3)

180   Parameters a-f were evaluated by fitting the frequencies of v_-, v_+ and D with pressure and

181   temperature using a TableCurve 3D V4.0 software package. The fitting results are listed in Table 1

182   and illustrated in Figures 6a-c. The residuals between the measured data and their fitted values are

183   less than 0.3, 0.4 and 0.2 cm^{-1} for v_-, v_+ and D, respectively. Our results show that the largest

184   pressure-dependent frequency shifts occur for the lower Fermi diad band v_- and the resonance

185   splitting D value of CO_2 in H_2O-CO_2±NaCl±CH_4 fluids, within the p-T range covered by our

186   experiment. Thus, the v_- and D frequency shifts are more suitable for pressure sensing in

187   aqueo-carbonic fluid systems.

188   **Discussion**

189   **Effect of temperature and pressure on the Fermi diad bands**

190   As can be seen from Figure 6a, within the p-T range of our experiment, v_- shifts to lower

191   frequencies with increasing pressure and to higher frequencies with increasing temperature, at

192   progressively lower $\partial v_-/\partial p$ and $\partial v_-/\partial T$ rates, respectively. Conversely, the effect of pressure on the

193   frequency shift of the v_+ band is weaker and non-monotonic (Fig. 6b): The v_+ band was observed to

194   shift to lower frequencies at low p-values and to higher frequencies with pressure at high p-values,

195   with a minimum between 400 to 500 MPa. Due to the nature of the variations in temperature and

196   pressure of the v_- and v_+ bands' frequencies, the D frequency value increases with pressure and

197   decreases with temperature in monotonic fashion, as shown in Fig. 6c.

Influence of fluid composition on the Raman peak positions

199   In most cases, natural aqueo-carbonic fluid inclusions contain CH_4, CO or N_2 in the carbonic and

200   electrolytes in the aqueous phase (Berkesi et al., 2009; Bersani et al., 2009; Giorgetti et al., 1996; Li

201   et al., 2014; Peng et al., 2014; Salvioli-Mariani et al., 2015; Thomas et al., 1990; Wang et al., 2013;

202   Zhu and Peng, 2015). In order to determine the pressures within these aqueo-carbonic fluid

203   inclusions using CO_2 as an internal pressure sensor, it is fundamentally important to ascertain the

204   influence of these additional components on the p-T-dependent behavior of the CO_2 Raman peak

205   position shifts.

206   The solubility of NaCl (as well as many other electrolytes) in CO_2 is lower by 5-7 orders of

207   magnitude than in H_2O (Zakirov et al., 2007) and thus can be neglected. However, the dissolved

208   NaCl in H_2O can not only reduce the mutual solubilities of H_2O and CO_2, but also interacts with

209   water molecules and influence water structure (Sun et al., 2010). In principle, at high temperatures

210   where the carbonic phase contains a high concentration of water and weak hydrogen bond is formed

211   between CO_2 and H_2O molecules, the addition of NaCl should have influence on the Fermi diad

212   bands' frequency. However, in our results (see Figures 4-6), within the error ranges, there is no

213   measurable difference in the p-T-dependence of the Fermi diad bands' frequencies measured from

214   Sample I (no NaCl) and II (with ~10 wt% NaCl). We think this probably because the dissolved NaCl

215   in Sample II is ~10 wt% and its effect on the CO_2 Fermi diad bands' frequency is insignificant. The

216   presence of CH_4 in the carbonic phase will reduce the CO_2 partial pressure, potentially leading to an

217   underestimation of the p- and T-dependent rates of the Fermi diad bands' vibrational frequencies.

218   Nevertheless, the influence of CH_4 on the Fermi diad band peak positions is negligible, provided that

219   the CH_4 content is no more than 10 mol% (Seitz et al., 1996). This is confirmed from our Raman

220   measurements (see Figure 6) showing that the difference between the Fermi diad band peak positions

221   measured from Sample I (with ~10 mol% CH_4) and III (no CH_4) is negligible within the estimated

222   errors.

223   **Determination of pressure from CO_2 Raman frequency shifts**

224   Based on the systematic frequency shifts of v_- and D with pressure and temperature, for which

225   we have demonstrated that small amounts of CH_4 in the carbonic phase (~10 mol%) and NaCl in the

226   aqueous phase (~ 10 wt%) have no measureable effect, the total pressure (in MPa) of aqueo-carbonic

227   (H_2O-CO_2±NaCl±CH_4) fluid inclusions at elevated temperatures can be determined, by using the

228   following two polynomial equations:

229         $p = -16 + 1.232 \times T - 53.72 \times (\Delta v_-) - 1.83 \times 10^{-3} \times T^2 + 24.46 \times (\Delta v_-)^2 - 0.292 \times T \times (\Delta v_-)$, $R^2 = 0.9962$;

230   (4a)

231         $p = -26 + 1.501 \times T + 193.24 \times (\Delta D) - 1.61 \times 10^{-3} \times T^2 + 5.436 \times (\Delta D)^2 + 0.158 \times T \times (\Delta D)$, $R^2 = 0.9976$.

232   (4b)

233   where $\Delta v_- = v_{-p} - 1281.56$ cm^{-1} and $\Delta D = D_p - 104.07$ cm^{-1}, representing the frequency shifts of v_-

234   and D, respectively, relative to the reference values measured at 23°C and 6 MPa, at which point

235   vapor and liquid CO_2 are in equilibrium. Equations 4a and 4b can be used at $22 \leq T \leq 400$ °C and

236   pressures up to 1200 MPa, with uncertainties of better than 50 MPa and 40 MPa for the pressure

237   determined from v_- and D, respectively (Fig. 7).

238   **Application to fluid inclusion research**

239   All of the Raman spectra in our experiments were measured from high-density (higher than CO_2

240   critical density) aqueo-carbonic fluids. Therefore, the applicability of equations 4a and 4b for

241   pressure determination holds only for aqueo-carbonic fluid inclusions containing a liquid carbonic

242   phase. The presence of <10 mol% CH_4 or <10 wt% NaCl will not affect the results significantly, but

243   higher concentrations of such volatiles or electrolytes may lead to the estimated pressure being

244   different from real values. In addition, the inclusions selected for study need to be sufficiently large

245   (i.e. >10 μm) and close to the surface, in order to optimize the Raman signal particularly at high

246   temperatures where instabilities in the CO_2-H_2O phase boundaries are encountered (Burke, 2001).

247   Due to the rapidly increasing internal pressure with rising temperature, decrepitation of such

248   inclusions is very common (Bodnar, 2003; Bodnar et al., 1989). This problem can be avoided by

249   heating the inclusions within a HDAC or other similar high-pressure, high-temperature instruments

250   (Darling and Bassett, 2002; Schmidt et al., 1998). As pressure within the fluid inclusions and in the

251   HDAC sample chamber are increased jointly with temperature, the pressure gradient from within the

252   inclusion to the host mineral is greatly reduced and decrepitation can be prevented.

253   After an appropriate aqueo-carbonic fluid inclusion within an assemblage has been selected for

254   probing, the second step is to determine the Raman peak positions of CO_2 at a known reference p-T

255   condition (e.g., 22 °C and 6 MPa). This is straightforward for a V+L_{car}+L_{aq} inclusion as its pressure

256   can be estimated from the CO_2 vapor-liquid equilibrium pressure, whereas for a L_{car}+L_{aq} inclusion

257   with unknown pressure at room temperature, we can either determining its reference pressure using a

258   microthermometric method, or as an optional choice, determining the reference peak positions by

259   additional Raman scattering measurements with the same settings of a V+L_{car}+L_{aq} inclusion. This

260 step is critical for the usage of Equation 4a because different Raman scattering or calibration settings

261 will affect the measured Raman peak positions to a significant degree. As for the usage of Equation

262 4b, this step is suggested but not required because the relationship between D and CO_2 density or

263 pressure has been proven to be quite reproducible (Fall et al., 2011; Kawakami et al., 2003; Rosso

264 and Bodnar, 1995; Song et al., 2009; Wang et al., 2011; Yamamoto and Kagi, 2006).

265   In the third step, Raman spectra of the carbonic phase in the target aqueo-carbonic fluid

266 inclusion should be measured from room to its homogenization temperature with proper intervals.

267 During this part of the procedure, measurement of a Raman signal from an external source for

268 spectral calibration is strongly recommended as the heat from the HDAC or heating stage will

269 significantly affect the measured Raman peak positions. In the final step, Δv_- or ΔD at different

270 temperatures are calculated and the total pressure in the target inclusion is determined either from Δv_-

271 using Equation 4a or from ΔD using Equation 4b. Compared with v_-, which may be affected by some

272 unexpected errors, pressures calculated from D appear to be more reliable as the frequency shifts of

273 v_- and v_+ are usually affected by those unexpected errors in the same manner.

Implications

275   The use of microthermometry for estimation of pressure in natural H_2O-CO_2 fluid inclusions is

276 often limited by the presence of additional volatiles, such as CH_4 and CO, and electrolytes such as

277 NaCl. We have made a systematic in situ Raman study of H_2O-CO_2 fluids, with and without CH_4 or

278 NaCl, using the HDAC within the p-T range of 22 °C $\leq T \leq$ 400 °C and $5 \leq p \leq 1200$ MPa, in order

279 to develop the use of CO_2 as an internal sensor for monitoring the pressure of aqueo-carbonic fluid

280 inclusions. We have determined the frequency shifts of the Fermi diad bands of CO_2 in

281 H_2O-$CO_2\pm NaCl\pm CH_4$ fluids as a function of pressure and temperature and, from these measurements,

282   closely examined the effect of CH_4 or NaCl on these shifts. The *p-T*-dependencies of the frequency

283   shifts of the lower Fermi diad band v_- and the resonant splitting D between the upper Fermi diad

284   band v_+ and v_- of CO_2 in aqueo-carbonic fluids were found to be monotonic, easily measurable and

285   quantifiable so as to be suitable for use as an internal pressure sensor.

286   Based on the quantified relationships of the frequency shifts of the Fermi diad bands with

287   temperature and total pressure, two polynomial equations were derived for the first time, for the

288   lower Fermi diad band v_- and the splitting D value, that can be used for determining the total pressure

289   in aqueo-carbonic fluid inclusions from ambient pressure to 1200 MPa. Our method is applicable for

290   aqueo-carbonic fluid inclusions containing a liquid carbonic phase and is recommended for content

291   levels <10 mol% CH_4 or <10 wt% NaCl. The use of CO_2 as an internal pressure sensor as developed

292   using our quantification procedure provides a more straightforward and more reliable method than

293   by the use of microthermometry for determining the pressure of natural aqueo-carbonic fluid

294   inclusions under elevated *p-T* conditions. As better pressure sensors with a better pressure resolution

295   are developed, higher-precision Raman instruments having greater signal sensitivity are produced

296   and more CO_2 Raman data are measured from aqueo-carbonic systems, the CO_2 Raman pressure

297   sensor will become more accurate for work on fluid inclusions in the future.

298   **Acknowledgements**

References

302

303 Akinfiev, N.N., and Diamond, L.W. (2010) Thermodynamic model of aqueous CO_2–H_2O–NaCl solutions from −22 to
304   100°C and from 0.1 to 100MPa. Fluid Phase Equilibria, 295(1), 104-124.

305 Aranovich, L.Y., Zakirov, I., Sretenskaya, N., and Gerya, T. (2010) Ternary system H_2O-CO_2-NaCl at high *T-P*
306   parameters: An empirical mixing model. Geochemistry International, 48(5), 446-455.

307 Azbej, T., Severs, M.J., Rusk, B.G., and Bodnar, R.J. (2007) In situ quantitative analysis of individual H_2O–CO_2 fluid
308   inclusions by laser Raman spectroscopy. Chemical Geology, 237(3–4), 255-263.

309 Bakker, R.J., and Diamond, L.W. (2000) Determination of the composition and molar volume of H_2O-CO_2 fluid
310   inclusions by microthermometry. Geochimica et Cosmochimica Acta, 64(10), 1753-1764.

311 Bassett, W., Shen, A., Bucknum, M., and Chou, I.M. (1993) A new diamond anvil cell for hydrothermal studies to 2.5
312   GPa and from −190 to 1200 °C. Review of Scientific Instruments, 64(8), 2340-2345.

313 Berkesi, M., Hidas, K., Guzmics, T., Dubessy, J., Bodnar, R.J., Szabó, C., Vajna, B., and Tsunogae, T. (2009) Detection

314   of small amounts of H_2O in CO_2-rich fluid inclusions using Raman spectroscopy. Journal of Raman
315   Spectroscopy, 40(11), 1461-1463.

316 Bersani, D., Salvioli-Mariani, E., Mattioli, M., Menichetti, M., and Lottici, P.P. (2009) Raman and micro-thermometric
317   investigation of the fluid inclusions in quartz in a gold-rich formation from Lepaguare mining district (Honduras,
318   Central America). Spectrochimica Acta Part A: Molecular and Biomolecular Spectroscopy, 73(3), 443-449.

319 Bodnar, R.J. (2003) Reequilibration of fluid inclusions. In A.A. Samson, and D. Marshall, Eds. Fluid inclusions: Analysis
320   and interpretation, 32, p. 213-230. Mineral. Assoc. Canada.

321 Bodnar, R.J., Binns, P.R., and Hall, D.L. (1989) Synthetic fluid inclusions‐VI. Quantitative evaluation of the

322   decrepitation behaviour of fluid inclusions in quartz at one atmosphere confining pressure. Journal of
323   Metamorphic Geology, 7(2), 229-242.

324 Burke, E.A.J. (2001) Raman microspectrometry of fluid inclusions. Lithos, 55(1–4), 139-158.

325 Chen, Y., Zhou, Y., and Ni, P. (2006) A new method for measurement of internal pressure of inclusions: CO_2-Raman
326   spectrometry. Rock and Mineral Analysis, 25(3), 211-214.

327 Chi, G., Dubé, B., Williamson, K., and Williams-Jones, A. (2006) Formation of the Campbell-Red Lake gold deposit by
328   H_2O-poor, CO_2-dominated fluids. Mineralium Deposita, 40(6-7), 726-741.

329 Darling, R.S., and Bassett, W.A. (2002) Analysis of natural H_2O+ CO_2+ NaCl fluid inclusions in the hydrothermal
330   diamond anvil cell. American Mineralogist, 87(1), 69-78.

331 Diamond, L.W. (1996) Isochoric paths in immiscible fluids and the interpretation of multicomponent fluid inclusions.
332   Geochimica et Cosmochimica Acta, 60(20), 3825-3834.

333 Diamond, L.W. (2001) Review of the systematics of CO_2–H_2O fluid inclusions. Lithos, 55(1–4), 69-99.

334 Fall, A., Tattitch, B., and Bodnar, R.J. (2011) Combined microthermometric and Raman spectroscopic technique to
335   determine the salinity of H_2O–CO_2–NaCl fluid inclusions based on clathrate melting. Geochimica et
336   Cosmochimica Acta, 75(4), 951-964.

337 Garrabos, Y., Echargui, M.A., and Marsault-Herail, F. (1989) Comparison between the density effects on the levels of the

338   Raman spectra of the Fermi resonance doublet of the $^{12}C^{16}O_2$ and $^{13}C^{16}O_2$ molecules. The Journal of Chemical
339   Physics, 91(10), 5869-5881.

340 Garrabos, Y., Tufeu, R., Le Neindre, B., Zalczer, G., and Beysens, D. (1980) Rayleigh and Raman scattering near the
341   critical point of carbon dioxide. The Journal of Chemical Physics, 72(8), 4637-4651.

342   Giorgetti, G., Frezzotti, M.L.E., Palmeri, R., and Burke, E.A.J. (1996) Role of fluids in migmatites: CO_2-H_2O fluid
343   inclusions in leucosomes from the Deep Freeze Range migmatites (Terra Nova Bay, Antarctica). Journal of
344   Metamorphic Geology, 14(3), 307-317.
345   Gordon, H.R., and McCubbin, T.K. (1966) The 2.8-micron bands of CO_2. Journal of Molecular Spectroscopy, 19,
346   137-154.
347   Guo, H., Chen, Y., Hu, Q., Lu, W., Ou, W., and Geng, L. (2014) Quantitative Raman spectroscopic investigation of
348   geo-fluids high-pressure phase equilibria: Part I. Accurate calibration and determination of CO_2 solubility in
349   water from 273.15 to 573.15K and from 10 to 120MPa. Fluid Phase Equilibria, 382(0), 70-79.
350   Holloway, J.R., Burnham, C.W., and Millhollen, G.L. (1968) Generation of H_2O-CO_2 Mixtures for Use in Hydrothermal
351   Experimentation. Journal of Geophysical Research, 73(20), 6598-6600.
352   Hurai, V. (2010) Fluid inclusion geobarometry: Pressure corrections for immiscible H_2O–CH_4 and H_2O–CO_2 fluids.
353   Chemical Geology, 278(3–4), 201-211.
354   Kawakami, Y., Yamamoto, J., and Kagi, H. (2003) Micro-Raman Densimeter for CO_2 Inclusions in Mantle-Derived
355   Minerals. Applied spectroscopy, 57(11), 1333-1339.
356   Li, N., Chen, Y.-J., Deng, X.-H., and Yao, J.-M. (2014) Fluid inclusion geochemistry and ore genesis of the Longmendian
357   Mo deposit in the East Qinling Orogen: Implication for migmatitic-hydrothermal Mo-mineralization. Ore
358   Geology Reviews, 63, 520-531.
359   Lowenstern, J. (2001) Carbon dioxide in magmas and implications for hydrothermal systems. Mineralium Deposita,
360   36(6), 490-502.
361   Mao, S., Duan, Z., and Hu, W. (2009) A vapor–liquid phase equilibrium model for binary CO_2–H_2O and CH_4–H_2O
362   systems above 523K for application to fluid inclusions. The Journal of Supercritical Fluids, 50(1), 13-21.
363   Mao, S., Hu, J., Zhang, D., and Li, Y. (2013) Thermodynamic modeling of ternary CH_4-H_2O-NaCl fluid inclusions.
364   Chemical Geology, 335(0), 128-135.
365   Mumm, A.S., Oberthür, T., Vetter, U., and Blenkinsop, T.G. (1997) High CO_2 content of fluid inclusions in gold
366   mineralisations in the Ashanti Belt, Ghana: a new category of ore forming fluids? Mineralium Deposita, 32(2),
367   107-118.
368   Peng, Y., Gu, X., Zhang, Y., Liu, L., Wu, C., and Chen, S. (2014) Ore-forming process of the Huijiabao gold district,
369   southwestern Guizhou Province, China: Evidence from fluid inclusions and stable isotopes. Journal of Asian
370   Earth Sciences, 93, 89-101.
371   Phillips, G., and Evans, K. (2004) Role of CO_2 in the formation of gold deposits. Nature, 429(6994), 860-863.
372   Rosso, K.M., and Bodnar, R.J. (1995) Microthermometric and Raman spectroscopic detection limits of CO_2 in fluid
373   inclusions and the Raman spectroscopic characterization of CO_2. Geochimica et Cosmochimica Acta, 59(19),
374   3961-3975.
375   Salvioli-Mariani, E., Toscani, L., Boschetti, T., Bersani, D., and Mattioli, M. (2015) Gold mineralisations in the Canan
376   area, Lepaguare District, east-central Honduras: Fluid inclusions and geochemical constraints on gold deposition.
377   Journal of Geochemical Exploration, 158, 243-256.
378   Schmidt, C., Chou, I., Bodnar, R.J., and Bassett, W.A. (1998) Microthermometric analysis of synthetic fluid inclusions in
379   the hydrothermal diamond-anvil cell. American Mineralogist, 83, 995-1007.
380   Schmidt, C., Rosso, K.M., and Bodnar, R.J. (1995) Synthetic fluid inclusions: XIII. Experimental determination of PVT
381   properties in the system H_2O+ 40 wt % NaCl + 5 mol% CO_2 at elevated temperature and pressure. Geochimica
382   et Cosmochimica Acta, 59(19), 3953-3959.
383   Schmidt, C., and Ziemann, M.A. (2000) In-situ Raman spectroscopy of quartz: A pressure sensor for hydrothermal
384   diamond-anvil cell experiments at elevated temperatures. American Mineralogist, 85(11-12), 1725-1734.

385 Seitz, J.C., Pasteris, J.D., and Chou, I.-M. (1996) Raman spectroscopic characterization of gas mixtures. II. Quantitative
386   composition and pressure determination of the CO_2-CH_4 system. American Journal of Science, 296(6), 577-600.

387 Shmulovich, K.I., and Graham, C.M. (1999) An experimental study of phase equilibria in the system H_2O-CO_2-NaCl at
388   800°C and 9 kbar. Contributions to mineralogy and petrology, 136(3), 247-257.

389 Shmulovich, K.I., and Graham, C.M. (2004) An experimental study of phase equilibria in the systems H_2O–CO_2–$CaCl_2$
390   and H_2O–CO_2–NaCl at high pressures and temperatures (500–800°C, 0.5–0.9 GPa): geological and geophysical
391   applications. Contributions to Mineralogy and Petrology, 146(4), 450-462.

392 Song, Y., Chou, I.M., Hu, W., Robert, B., and Lu, W. (2009) CO_2 Density-Raman Shift Relation Derived from Synthetic

393   Inclusions in Fused Silica Capillaries and Its Application. Acta Geologica Sinica-English Edition, 83(5),

394   932-938.

395 Stoicheff, B.P. (1958) High Resolution Raman Spectroscopy of Gases: XI. Spectra of CS_2 and CO_2. Canadian Journal of
396   Physics, 36(2), 218-230.

397 Sun, Q., Zhao, L., Li, N., and Liu, J. (2010) Raman spectroscopic study for the determination of Cl^- concentration
398   (molarity scale) in aqueous solutions: Application to fluid inclusions. Chemical Geology, 272(1), 55-61.

399 Thomas, A.V., Pasteris, J.D., Bray, C.J., and Spooner, E.T.C. (1990) H_2O-CH_4-NaCl-CO_2 inclusions from the footwall
400   contact of the Tanco granitic pegmatite: Estimates of internal pressure and composition from microthermometry,
401   laser Raman spectroscopy, and gas chromatography. Geochimica et Cosmochimica Acta, 54(3), 559-573.

402 Thomas, A.V., and Spooner, E.T.C. (1992) The volatile geochemistry of magmatic H_2O-CO_2 fluid inclusions from the
403   Tanco zoned granitic pegmatite, southeastern Manitoba, Canada. Geochimica et Cosmochimica Acta, 56(1),
404   49-65.

405 Tsunogae, T., Santosh, M., Osanai, Y., Owada, M., Toyoshima, T., and Hokada, T. (2002) Very high-density carbonic
406   fluid inclusions in sapphirine-bearing granulites from Tonagh Island in the Archean Napier Complex, East
407   Antarctica: implications for CO_2 infiltration during ultrahigh-temperature (T>1,100 °C) metamorphism.
408   Contributions to Mineralogy and Petrology, 143(3), 279-299.

409 Wang, C.H., and Wright, R.B. (1973) Raman studies of the effect of density of the fermi resonance in CO_2. Chemical
410   Physics Letters, 23(2), 241-246.

411 Wang, G.-G., Ni, P., Wang, R.-C., Zhao, K.-D., Chen, H., Ding, J.-Y., Zhao, C., and Cai, Y.-T. (2013) Geological, fluid
412   inclusion and isotopic studies of the Yinshan Cu–Au–Pb–Zn–Ag deposit, South China: Implications for ore
413   genesis and exploration. Journal of Asian Earth Sciences, 74, 343-360.

414 Wang, H., and Zheng, H. (2012) Research on Raman Spectra of Oxalic Acid During Decarboxylation under High
415   Temperature and High Pressure. Spectroscopy and Spectral Analysis, 32(3), 669-672.

416 Wang, X., Chou, I., Hu, W., Burruss, R.C., Sun, Q., and Song, Y. (2011) Raman spectroscopic measurements of CO_2
417   density: Experimental calibration with high-pressure optical cell (HPOC) and fused silica capillary capsule
418   (FSCC) with application to fluid inclusion observations. Geochimica et Cosmochimica Acta, 75(14), 4080-4093.

419 Welsh, H.L., Pashler, P.E., and Stoicheff, B.P. (1952) Density Effects in the Spectrum of Carbon Dioxide. Canadian
420   Journal of Physics, 30(2), 99-110.

421 Williams-Jones, A., and Ferreira, D. (1989) Thermal metamorphism and H_2O-CO_2-NaCl immiscibility at Patapedia,
422   Quebec: evidence from fluid inclusions. Contributions to Mineralogy and Petrology, 102(2), 247-254.

423 Xu, G., and Pollard, P.J. (1999) Origin of CO_2-rich fluid inclusions in synorogenic veins from the Eastern Mount Isa Fold
424   Belt, NW Queensland, and their implications for mineralization. Mineralium Deposita, 34(4), 395-404.

425 Yamamoto, J., and Kagi, H. (2006) Extended micro-Raman densimeter for CO_2 applicable to mantle-originated fluid
426   inclusions. Chemistry letters, 35(6), 610-611.

427   Yamamoto, J., Kagi, H., Kawakami, Y., Hirano, N., and Nakamura, M. (2007) Paleo-Moho depth determined from the
428   pressure of CO_2 fluid inclusions: Raman spectroscopic barometry of mantle- and crust-derived rocks. Earth and
429   Planetary Science Letters, 253(3-4), 369-377.
430   Zakirov, I., Sretenskaja, N., Aranovich, L., and Volchenkova, V. (2007) Solubility of NaCl in CO_2 at high pressure and
431   temperature: First experimental measurements. Geochimica et Cosmochimica Acta, 71(17), 4251-4255.
432   Zhu, Y., and Peng, J. (2015) Infrared microthermometric and noble gas isotope study of fluid inclusions in ore minerals at
433   the Woxi orogenic Au–Sb–W deposit, western Hunan, South China. Ore Geology Reviews, 65, Part 1, 55-69.

434

435   Table 1. Parameters from fitting of the frequency positions of the CO_2 Fermi diad bands (v_+ and v_-)

436   and the v_+ and v_- splitting (D) values with pressure and temperature used to derive Equation 3 shown

437   in the text.

	a	b	c	$d \times 10^{-6}$	$e \times 10^{-6}$	$f \times 10^{-6}$	R^2
v_-	1281.37(4)	0.01077(5)	-0.00853(2)	-15.2(12)	3.24(16)	0.066(6)	0.9934
v_+	1385.63(5)	0.00427(6)	-0.00378(17)	-8.6(15)	2.85(21)	-1.3(7)	0.8717
D	104.17(2)	-0.00738(2)	0.00505(7)	9.9(7)	-0.41(9)	-2.0(3)	0.9971

438

439

440
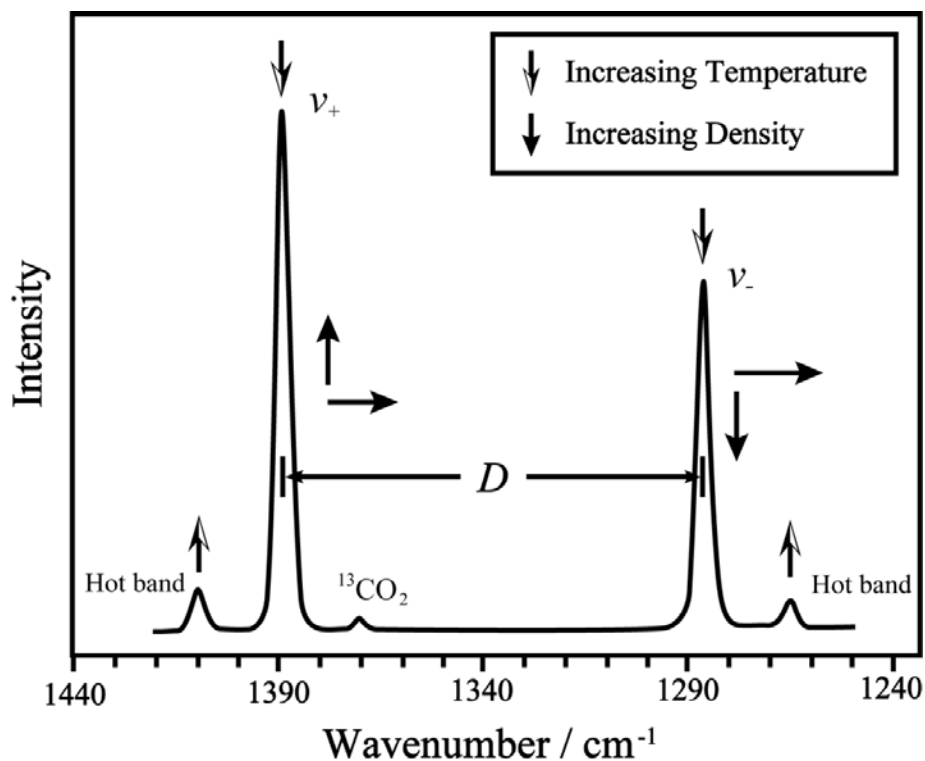
441

442   Figure 1. A typical Raman spectrum of CO_2 with the effects of density and temperature illustrated by

443   use of arrows, as modified from Rosso and Bodnar (1995).
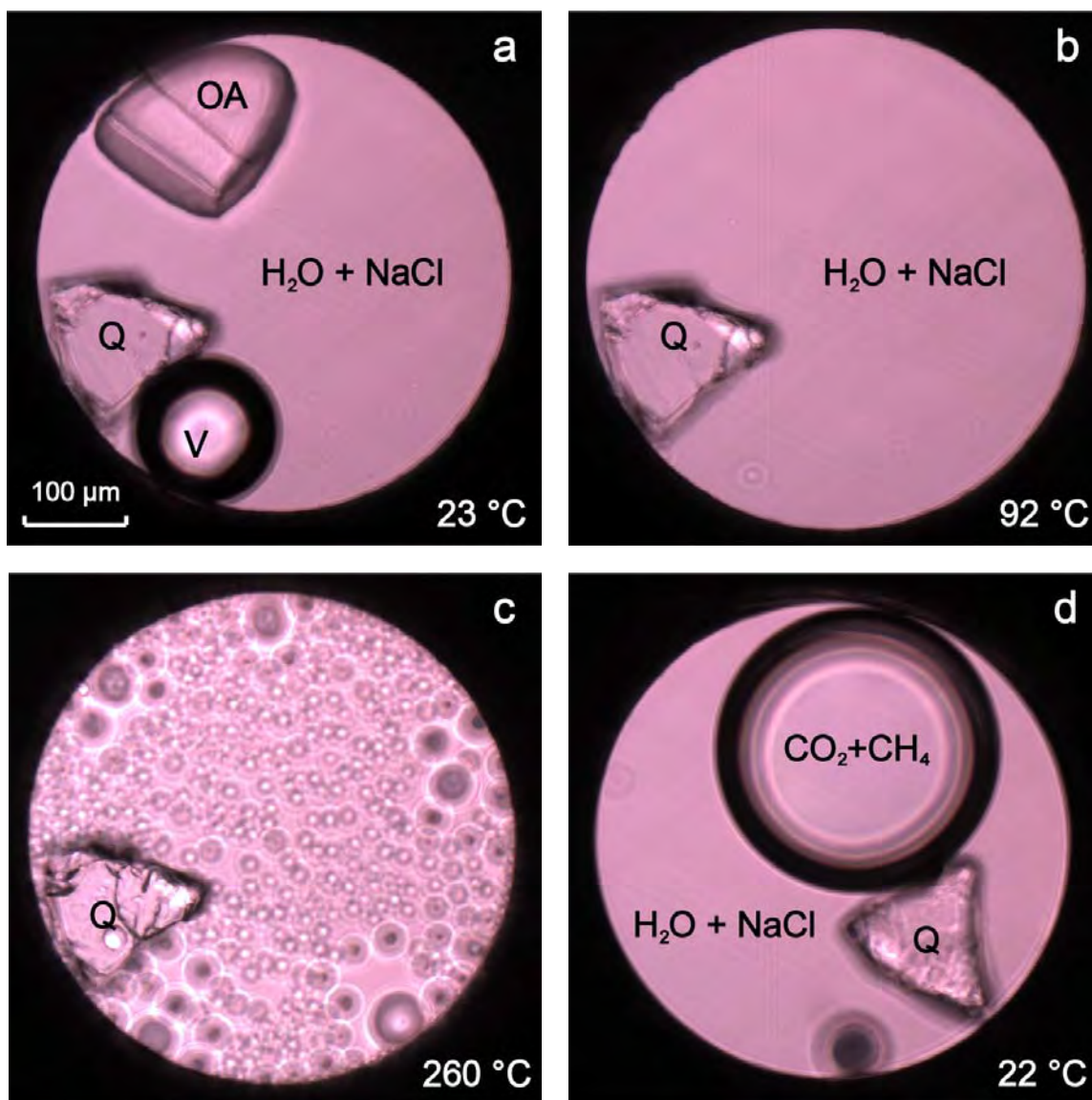
444

445

446   Figure 2. Photographs of the sample chamber at different temperatures for Sample II (see text):

447   (**a**) oxalic acid (OA, partly dissolved), H_2O+NaCl an air bubble (V) in the sealed sample chamber at

448   room temperature; (**b**) oxalic acid dissolved at 73 °C and the system homogenized at 92 °C; (**c**) CO_2

449   bubbles generated from the decomposition of oxalic acid at about 260 °C; (**d**) aqueous and

450   high-density carbonic fluid (90 mol% CO_2 and 10 mol% CH_4) coexist within the chamber after the

451   system was cooled down to 22 °C.
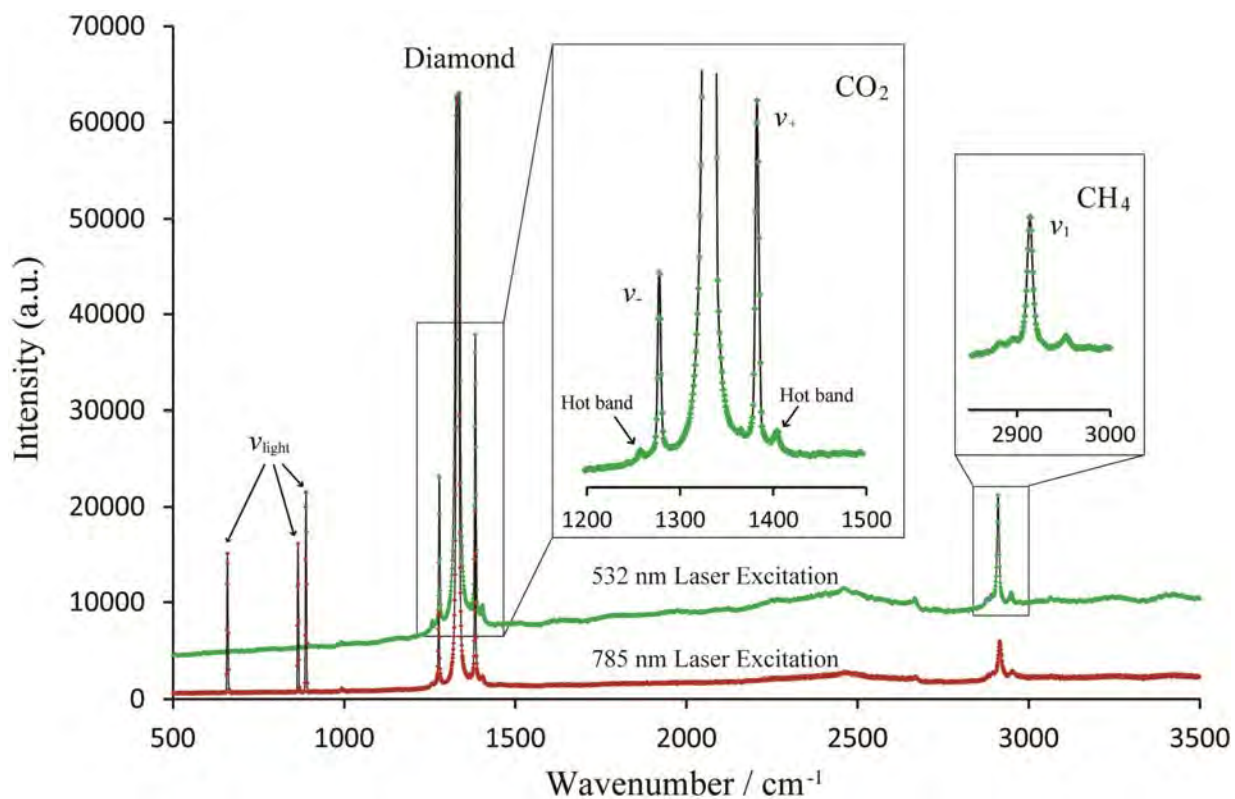
452

453   Figure 3. Raman spectra of the carbonic phase measured with 532nm and 785nm laser excitation,

454   respectively, at 23 °C and ~ 30 MPa in Sample II (see text). In the spectrum measured with 532 nm

455   laser excitation, the intensity of the CH_4 v_1 band (1.11×10^4) is about 38% of that of the CO_2 v_+ band

456   (2.92×10^4), and the corresponding CH_4 concentration in the carbonic phase, after taking into account

457   of the quantification factor ratio given by Seitz et al. (1996), was estimated to be ~10 mol%.

458
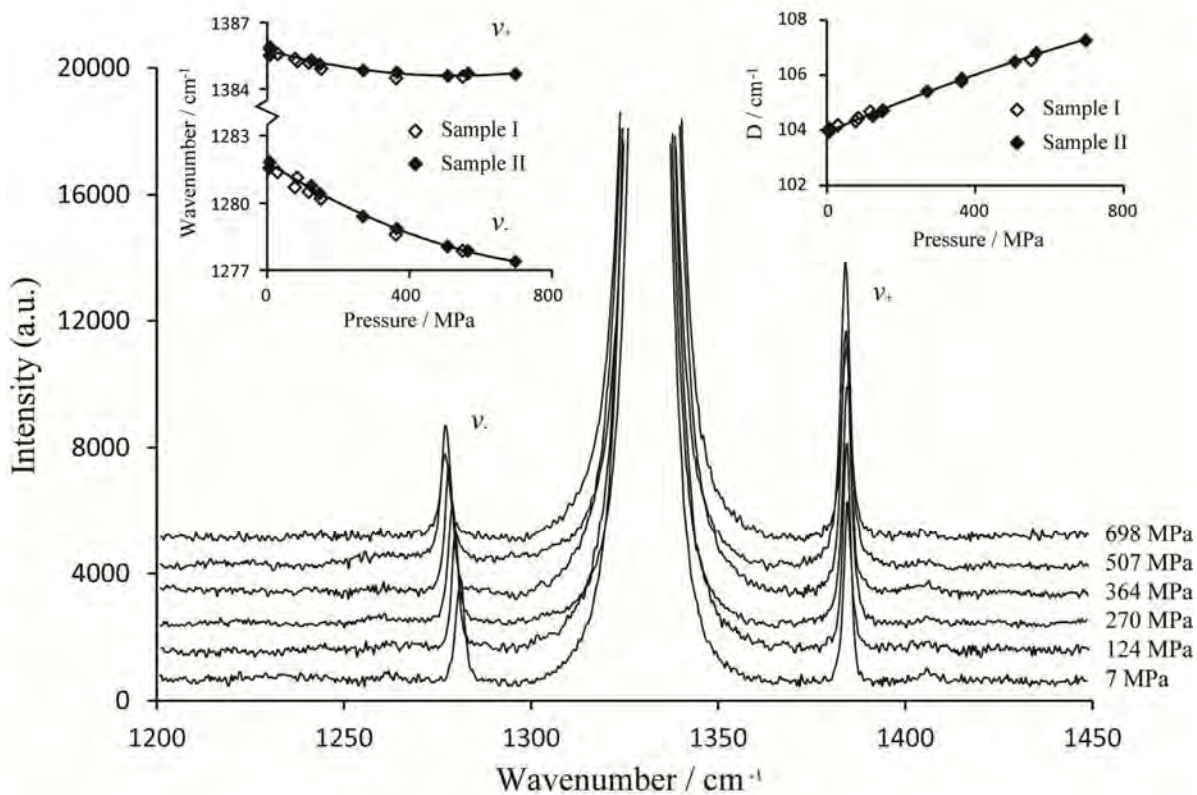
Figure 4. The effect of pressure on the Raman vibrational frequencies of CO_2 at 23 °C. The insets

show the frequency shifts of the CO_2 Fermi diad bands v_+ and v_- and the splitting D, as a function of

pressure for Sample I (open diamonds) and Sample II (solid diamonds). All spectra are shown after

baseline corrections and spectral calibrations were made.
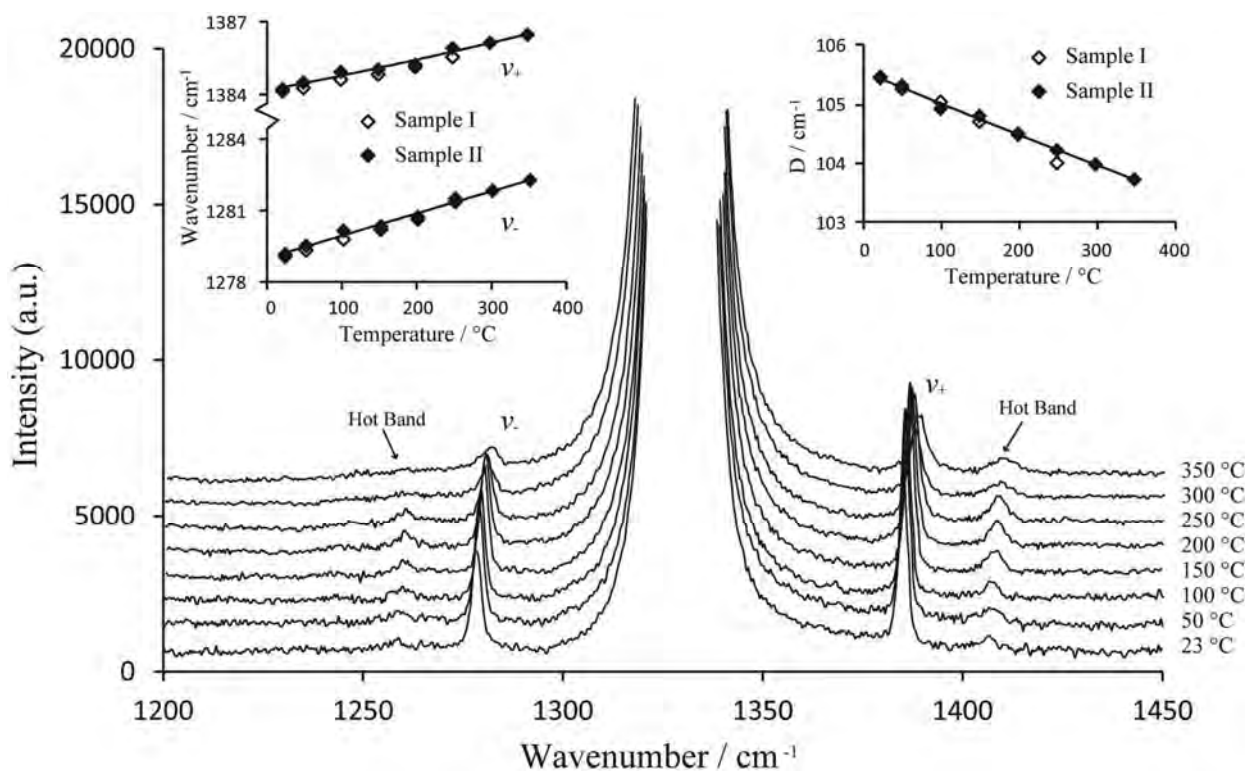
465

466 Figure 5. The effect of temperature on the Raman vibrational frequencies of CO_2 at approximately

467 200 MPa. The insets show the frequency shifts of the CO_2 Fermi diad bands v_+ and v_- and the

468 splitting D, as a function of temperature for Sample I (open diamonds) and Sample II (solid

469 diamonds). All spectra are shown after making baseline corrections, spectral calibrations and

470 pressure corrections (see text).

471

472

473

474
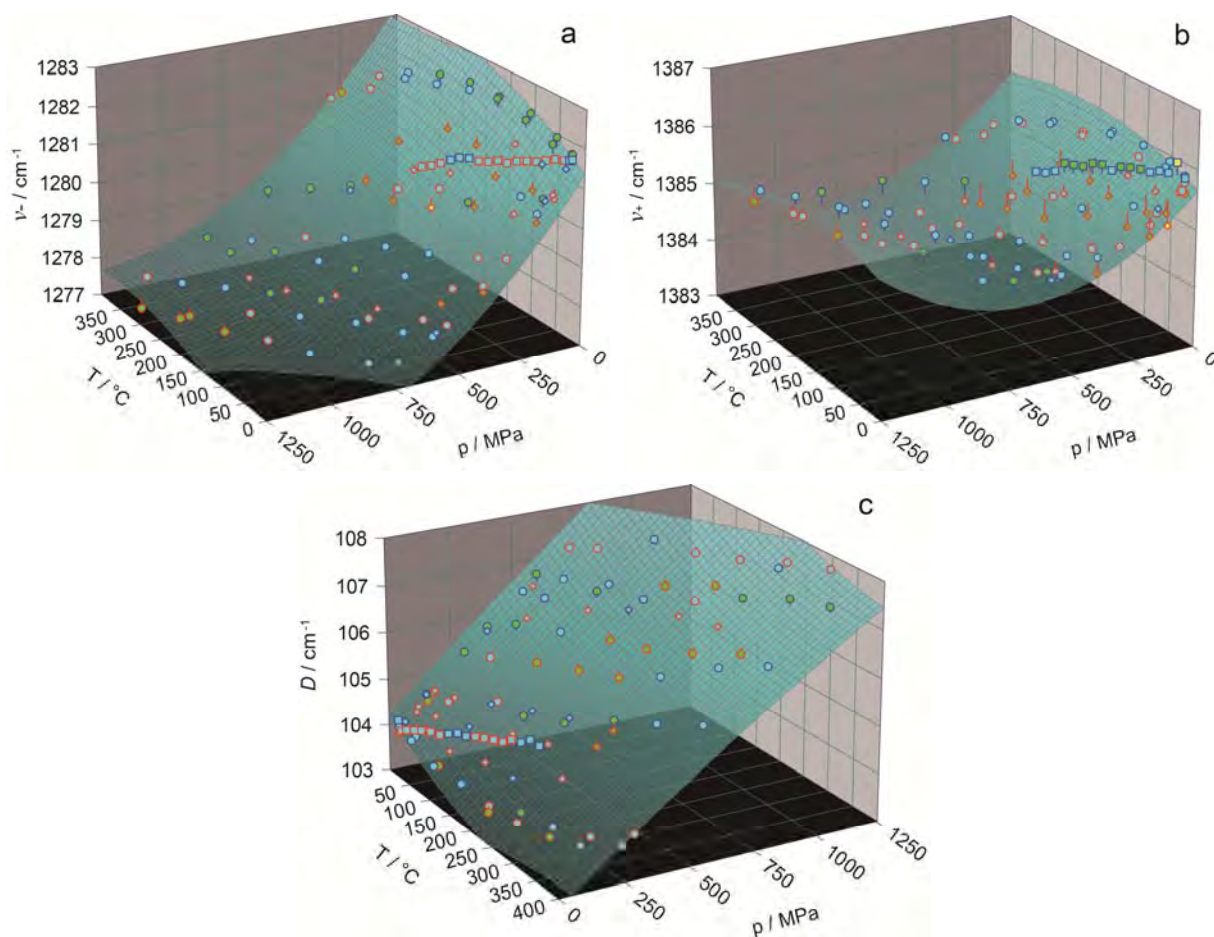
475

476

477 Figure 6. Fitting results of the CO_2 Raman vibrational frequencies (**a** for v_-, **b** for v_+) and D splitting

478 (**c**) with pressure and temperature. Diamonds, circles and squares represent data measured from

479 Sample I, II and III, respectively; border color represents the measured data that are higher (blue) or

480 lower (red) than their fitted values; filled color represents the error between measured data and fitted

481 value, blue is for error <0.1 cm^{-1}, green is for 0.1~0.2 cm^{-1} and yellow is for 0.2~0.4 cm^{-1}.

482
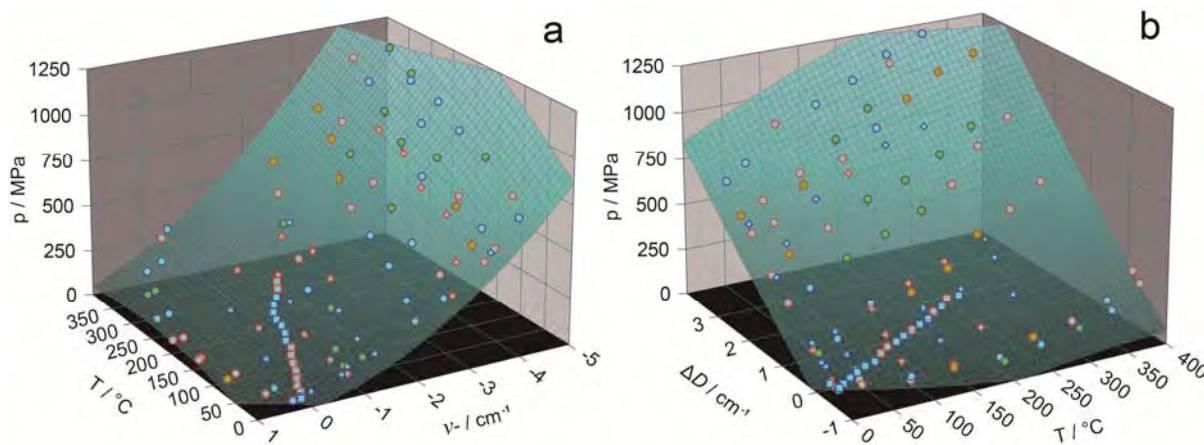
483

484 Figure 7. Pressure determination from the frequency shifts of v_- (**a**) and D (**b**) of CO_2 at different

485 temperatures. Diamonds, circles and squares represent data measured from Sample I, II or III,

486 respectively; border color represents the measured data that are higher (blue) or lower (red) than their

487 fitted values; filled color represents the errors between measured data and fitted value, blue is for

488 error less than 20 MPa and green is for error between 20 and 50 MPa.

Sample I

T/°C	p/Mpa	$v-$	$Iv-$	$v+$	$Iv+$	D	$\Delta v-$	ΔD
22	84	1280.82	6711	1385.26	11740	104.44	-0.74	0.37
50	109	1280.79	6410	1385.16	11390	104.37	-0.77	0.30
100	163	1280.85	5229	1385.24	9559	104.40	-0.72	0.33
150	250	1280.69	3719	1385.14	6963	104.45	-0.87	0.38
200	305	1280.51	2202	1384.98	4294	104.48	-1.06	0.41
250	408	1280.01	651	1384.63	1724	104.62	-1.55	0.55
22	78	1280.71	4119	1385.04	7541	104.33	-0.85	0.26
23	362	1278.71	3565	1384.48	6781	105.78	-2.86	1.71
50	478	1278.39	2543	1384.48	5158	106.10	-3.17	2.03
100	639	1278.12	2547	1384.49	5875	106.38	-3.45	2.31
150	714	1278.16	1168	1384.74	3398	106.58	-3.41	2.51
200	823	1278.04	1056	1384.66	2739	106.61	-3.52	2.54
250	887	1278.09	492	1384.69	1278	106.60	-3.47	2.53
22	151	1280.20	3791	1384.92	8116	104.72	-1.36	0.65
50	186	1280.27	3682	1384.97	6723	104.70	-1.29	0.63
100	249	1280.19	3839	1384.98	7306	104.79	-1.37	0.72
150	329	1279.92	2623	1384.78	4937	104.86	-1.64	0.79
200	390	1279.83	1252	1384.77	2751	104.94	-1.73	0.87
250	474	1279.85	575	1384.73	1493	104.88	-1.71	0.81
23	29	1281.38	5109	1385.56	9214	104.18	-0.18	0.11
50	72	1281.37	2865	1385.49	5223	104.12	-0.19	0.05
100	83	1281.57	3677	1385.52	6838	103.95	0.01	-0.12
150	142	1281.29	3806	1385.25	6768	103.96	-0.27	-0.11
200	166	1281.41	2436	1385.35	4487	103.94	-0.15	-0.13
250	274	1280.88	1234	1384.99	2335	104.12	-0.69	0.05
22	117	1280.71	3820	1385.39	7304	104.68	-0.85	0.61
22	550	1277.98	2167	1384.55	4764	106.56	-3.58	2.49

Sample II

T/°C	p/Mpa	$v-$	$Iv-$	$v+$	$Iv+$	D	$\Delta v-$	ΔD
23	7	1281.56	2077	1385.63	3523	104.07	0.00	0.00
50	12	1282.00	2708	1385.93	3722	103.94	0.43	-0.13
100	20	1282.29	2688	1385.99	4052	103.70	0.73	-0.37

150	48	1282.43	2377	1386.04	3750	103.61	0.86	-0.46
200	73	1282.52	1913	1385.82	3084	103.31	0.96	-0.76
250	101	1282.43	1925	1385.82	3126	103.39	0.87	-0.68
300	140	1282.23	1226	1385.61	2295	103.39	0.66	-0.68
350	169	1281.86	669	1385.37	1572	103.52	0.29	-0.55
400	284	1281.08	265	1385.03	729	103.95	-0.48	-0.12
23	270	1279.42	5865	1384.84	11800	105.42	-2.14	1.35
50	331	1279.34	5318	1384.74	10580	105.40	-2.23	1.33
100	434	1279.23	4496	1384.70	9167	105.47	-2.34	1.40
150	514	1279.14	3214	1384.66	7105	105.52	-2.42	1.45
200	587	1279.08	2542	1384.65	5938	105.57	-2.48	1.51
250	659	1278.87	1741	1384.69	4581	105.81	-2.69	1.74
300	794	1278.59	364	1384.72	1240	106.14	-2.97	2.07
22	7	1281.73	3224	1385.69	5492	103.97	0.17	-0.10
23	6	1281.56	3145	1385.52	5840	103.96	0.00	-0.11
50	30	1281.84	3546	1385.85	6695	104.01	0.28	-0.06
100	40	1282.14	3386	1385.81	5746	103.68	0.57	-0.39
150	56	1282.39	3306	1386.00	5730	103.61	0.82	-0.46
200	74	1282.32	2708	1385.77	4766	103.45	0.76	-0.62
250	115	1282.21	2049	1385.80	3804	103.59	0.64	-0.48
300	153	1282.08	820	1385.66	1820	103.58	0.52	-0.49
350	208	1281.57	591	1385.22	1447	103.64	0.01	-0.43
400	239	1281.18	121	1384.95	378	103.77	-0.38	-0.30
23	507	1278.09	5268	1384.59	12140	106.50	-3.48	2.43
50	550	1278.08	4556	1384.53	10030	106.45	-3.48	2.38
100	674	1277.91	4010	1384.66	9081	106.75	-3.65	2.68
150	774	1278.13	3171	1384.88	7697	106.74	-3.43	2.68
200	890	1278.08	1232	1384.94	2979	106.86	-3.48	2.79
250	985	1277.97	928	1385.07	2239	107.10	-3.59	3.03
300	1077	1277.84	546	1385.10	1365	107.27	-3.73	3.20
350	1138	1277.71	302	1385.02	801	107.31	-3.85	3.24
23	564	1277.89	5625	1384.70	10140	106.82	-3.68	2.75
50	629	1277.88	4265	1384.67	9219	106.79	-3.68	2.72

100	725	1277.86	4119	1384.72	9172	106.86	-3.70	2.79
150	860	1277.84	3243	1384.77	6750	106.94	-3.73	2.87
200	970	1277.68	2515	1384.80	5898	107.12	-3.88	3.05
250	1129	1277.45	1814	1385.04	5179	107.59	-4.12	3.52
23	698	1277.41	2697	1384.67	5962	107.26	-4.15	3.19
50	767	1277.28	2777	1384.60	5882	107.32	-4.29	3.25
100	908	1277.35	2476	1384.96	5414	107.62	-4.22	3.55
150	985	1277.39	1789	1384.92	4342	107.54	-4.17	3.47
200	1073	1277.35	1490	1384.91	3653	107.56	-4.21	3.49
250	1166	1277.43	916	1385.11	2482	107.68	-4.13	3.61
300	1241	1277.42	579	1385.14	1643	107.73	-4.14	3.66
22	364	1278.88	4992	1384.75	9215	105.87	-2.69	1.80
50	433	1278.70	5329	1384.71	10170	106.01	-2.87	1.94
100	529	1278.77	4648	1384.80	9347	106.02	-2.79	1.95
150	639	1278.73	4853	1384.75	9295	106.02	-2.83	1.95
200	696	1278.64	1921	1384.69	4693	106.05	-2.92	1.98
250	786	1278.65	1470	1384.80	4072	106.15	-2.91	2.08
300	881	1278.38	1107	1384.70	2833	106.32	-3.18	2.25
350	892	1278.44	475	1384.79	1340	106.35	-3.12	2.28
22	148	1280.43	4225	1385.11	6908	104.69	-1.14	0.62
22	124	1280.78	4978	1385.29	8297	104.51	-0.78	0.44
50	160	1280.69	3376	1385.31	6120	104.62	-0.88	0.55
100	275	1280.34	3321	1385.14	5682	104.80	-1.23	0.73
150	295	1280.36	1774	1385.13	3333	104.78	-1.21	0.71
200	369	1280.11	1351	1384.96	2673	104.85	-1.46	0.78
250	475	1279.97	1137	1385.07	2360	105.10	-1.59	1.03
300	551	1279.66	822	1384.89	1832	105.23	-1.90	1.17
350	639	1279.35	565	1384.77	1079	105.42	-2.21	1.35

Sample III

22	5	1281.58	4119	1385.87	9502	104.21	0.01	0.06
25	10	1281.54	5122	1385.62	11580	104.00	-0.02	-0.15
31	20	1281.51	8949	1386.10	17130	104.03	-0.05	-0.12
42	35	1281.49	8659	1385.89	16720	104.09	-0.08	-0.06

52	50	1281.41	8895	1385.89	17110	104.12	-0.15	-0.03
63	68	1281.33	8727	1385.84	16210	104.14	-0.24	-0.01
74	86	1281.30	8224	1385.85	15700	104.12	-0.27	-0.03
85	104	1281.24	7799	1385.84	14900	104.20	-0.33	0.05
96	122	1281.14	7043	1385.82	14000	104.26	-0.43	0.11
106	140	1281.15	7223	1385.73	14080	104.24	-0.41	0.09
117	158	1281.07	5871	1385.80	11530	104.27	-0.49	0.13
128	176	1281.04	5122	1385.79	10760	104.29	-0.52	0.14
139	194	1281.06	6130	1385.69	12430	104.30	-0.51	0.15
150	212	1281.03	6405	1385.68	12090	104.31	-0.54	0.16
160	230	1280.93	5407	1385.68	11300	104.38	-0.64	0.24
171	248	1280.80	3435	1385.51	7705	104.39	-0.77	0.24
182	266	1280.68	2835	1385.45	6779	104.49	-0.89	0.34
193	284	1280.60	1430	1385.43	3464	104.40	-0.97	0.25